Ab initio calculation of inter-atomic decay rates of excited doubly ionized states in clusters

Přemysl Kolorenč

Institute of Theoretical Physics, Faculty of Mathematics and Physics, Charles University in Prague, V Holešovičkách 2, 180 00, Prague, Czech Republic

Vitali Averbukh

Max Planck Institute for the Physics of Complex Systems, Nöthnitzer Str. 38, D-01187, Dresden, Germany

Kirill Gokhberg and Lorenz S. Cederbaum

Theoretische Chemie, PCI, Universität Heidelberg, Im Neuenheimer Feld 229, D-69120, Heidelberg, Germany

(Dated: November 12, 2008)

Abstract

Recently, a computational technique for *ab initio* calculation of the inter-atomic and inter-molecular non-radiative decay processes has been developed [1]. It combines the Fano formalism with the Green's function method known as the algebraic diagrammatic construction. The problem of normalization of continuum wave functions stemming from the use of the Gaussian basis sets is solved by using the Stieltjes imaging technique. In the present paper, the methodology is extended in order to describe the inter-atomic decay of excited doubly ionized states of clusters. The new computational scheme is applied to compute the inter-atomic decay rates of doubly ionized states formed by Auger relaxation of core vacancies in NeAr and MgNe van der Waals clusters.

I. INTRODUCTION

Core ionization of an atom leads to Auger decay in which the vacancy is filled by one of the valence electrons and another valence electron is ejected to the continuum. On the other hand, inner-valence ionization of isolated atoms does not lead to decay by electron emission because of energetic constraints. In 1997, Cederbaum *et al.* [2] discovered a non-radiative decay mechanism characteristic of inner-valence vacancies in weakly bound clusters. It turns out that in clusters such an ionization can initiate a process called inter-atomic or inter-molecular Coulombic decay (ICD). In this process, the inner-valence vacancy is filled by an outer-valence electron and the excess energy is transferred to a neighboring species from which another electron is emitted. The ICD process is often interpreted as a transfer of virtual photon between the two cluster units. Unlike the Auger decay which is essentially intra-atomic, ICD is of inter-atomic nature and thus is strongly affected by the environment. Furthermore, the charge separation in the ICD final states usually leads to fragmentation of the cluster (Coulombic explosion). The theoretical predictions [2] were first confirmed experimentally by Marburger *et al.* [3] who studied the ICD process in Ne clusters. Jahnke *et al.* [4] provided very clear experimental proof for ICD in $2s$-ionized Ne dimers using electron-ion-ion coincidence spectroscopy in which the kinetic energy of the ICD electron and the total kinetic energy release (KER) between two Ne^+ ions were measured in coincidence. Another inter-atomic decay phenomenon, electron-transfer-mediated decay (ETMD), was later described by Zobeley *et al.* [5]. In ETMD, the initial vacancy is filled by an electron from a neighboring species. The secondary electron is ejected from the same or another neighboring species. Hence, the ETMD final states are characterized by the initially ionized atom being neutral at the end of the process. Consequences of ICD and related effects are of general relevance, in particular for understanding the multiple ionization and fragmentation of clusters upon exposure to high-energy radiation.

Rühl and co-workers investigated the fragmentation of argon clusters following their $2p$-shell ionization and clearly demonstrated the relevance of triple ionization processes [6]. An efficient mechanism for triple ionization of clusters following the absorption of a single x-ray photon, based on the ICD process, was later proposed by Santra and Cederbaum [7]. Let us consider the specific example of the neon dimer. For a neon atom Kelly [8] calculated that almost 30% of all dications produced in Auger decay of $Ne^+(1s^{-1})$ are highly excited,

possessing at least one hole in the $2s$ shell. This finding is in a good agreement with the measurement of Mehlhorn *et al.* [9] as well as with the more recent experimental study of Kádár *et al.* [10]. Still, the triple ionization threshold of a single neon atom is energetically too high for the autoionization of those states to be possible. In neon dimer, however, the possibility of the charge separation over both cluster subunits lowers the triple ionization threshold significantly and inter-atomic processes like ICD can occur – the $2s$ vacancy is filled by one of the now five $2p$ electrons of the atom which has undergone Auger decay and another electron is ejected from the $2p$ shell of the neighboring atom. The resulting trication then undergoes fragmentation. Santra and Cederbaum [7] not only showed that such a process is energetically possible but also proved that it is very efficient. Utilizing the CAP-CI (configuration interaction with complex absorbing potential) technique [11] they calculated a decay lifetime of about 80 fs for the one-site inner-valence excited states of the $(Ne_2)^{2+}$ dication. As in the case of singly ionized clusters other related processes such as ETMD can occur as well. The high efficiency and general relevance of the processes stimulated extensive experimental research. ICD from the Auger final states of a $2p$ vacancy in argon was unambiguously identified by Morishita *et al.* in argon dimers [12] and in ArKr [13] and more recently ICD in Ne dimer following the Auger decay of $Ne(1s^{-1})$ is being successfully studied [14–16].

No doubt, for a thorough understanding of the processes under consideration and for the theoretical simulation of measurable quantities such as the spectra of ICD electrons and the kinetic-energy release spectra of the ionic fragments, detailed knowledge of the relevant decay widths as a function of cluster geometry is essential. Averbukh and Cederbaum [1] developed an accurate and computationally efficient method for calculating the ICD decay widths of singly ionized clusters. It is based on the size-consistent and fast-convergent Green's function method known as algebraic diagrammatic construction (ADC) in combination with the Fano resonance formalism and Stieltjes imaging technique. The method proved to be superior to the Wigner-Weisskopf method [17] since effects like orbital relaxation, intra-atomic correlation, and channel coupling are fully taken into account. Furthermore, size-consistency (i.e., energy separability with respect to dissociation of a large system into multiple non-interacting fragments) and compactness of the matrices to diagonalize resulting from comparatively small explicit configuration space [18, 19] makes the ADC-based approach applicable even to large atomic or molecular clusters, for which alter-

native methods such as CAP-CI [20, 21] are not suitable. Still, in applications of the present method to extended systems attention has to paid to the fact that size-consistency in the dissociation limit need not necessarily ensure the proper size-intensive or size-extensive scaling of physical quantities. In contrast with order-by-order expansions, advanced Green's function methods such as ADC, which involve infinite partial summations of the diagrammatic perturbation series, may break another essential requirement for the correct scaling of physical quantities which is usually reffered to as charge consistency. It has been shown [22, 23] that an improper truncation in the many-body expansion of the propagator under consideration can yield a violation of the exact number of particles in the corresponding one-particle density.

The goal of the present work is to extend the ADC-based method to describe the interatomic decay of excited doubly ionized states of clusters. The theoretical aspects of the computational scheme are described in the next section. In Sec. III we report on the calculations of ICD and ETMD decay widths of excited states formed by Auger relaxation of core vacancies in NeAr and MgNe. The most important conclusions are summarized in Sec. IV.

II. THE METHOD

A. Fano formalism

In order to calculate the non-radiative decay widths of excited doubly ionized states of clusters we utilize the general approach introduced by Fano [24] and adapted by Howat *et al.* [25] to the specific case of Auger decay. The basic assumption is that at some energy E close to the energy E_{res} of the decaying state (resonance) the exact continuum wave function has the following "bound state in the continuum" character,

$$|\Psi_{\alpha,E}\rangle = a_\alpha(E)|\Phi\rangle + \sum_{\beta=1}^{N_c} \int C_{\beta,\alpha}(E,\epsilon)|\chi_{\beta,\epsilon}\rangle d\epsilon \qquad (\alpha = 1,\ldots,N_c) \tag{1}$$

with N_c being the number of open decay channels β and E_β are the corresponding threshold energies, $E_\beta < E$. In the present application the *discrete state* $|\Phi\rangle$ corresponds to the initial excited doubly ionized state with both holes located on the same cluster subunit while the decay channels β are triply ionized states characterized by specific three holes and the spin

state. The final states of an inter-atomic decay satisfy further condition that the three holes are distributed over more that one constituent of the cluster. The continuum wave functions are assumed to diagonalize the Hamiltonian,

$$\langle \chi_{\beta',\epsilon'}|H|\chi_{\beta,\epsilon}\rangle = (E_\beta + \epsilon)\delta_{\beta',\beta}\delta(E_{\beta'} + \epsilon' - E_\beta - \epsilon), \tag{2}$$

where H is the full Hamiltonian of the system. The orthogonality of the continuum to the discrete state is not required, $\langle\Phi|\chi_{\beta,\epsilon}\rangle \neq 0$. This makes the Fano theory very flexible with respect to approximating the discrete and continuum wave functions.

Inserting the Fano ansatz (1) into the Schrödinger equation $(H-E)|\Psi_{\alpha,E}\rangle = 0$ yields

$$\begin{aligned} (E_\Phi - E)a_\alpha(E) + \sum_{\beta=1}^{N_c}\int M_\beta(E,\epsilon)C_{\beta,\alpha}(E,\epsilon)d\epsilon &= 0 \\ a_\alpha(E)M^*_\beta(E,\epsilon) + (E_\beta + \epsilon - E)C_{\beta,\alpha}(E,\epsilon) &= 0 \qquad (\beta = 1,\ldots,N_c). \end{aligned} \tag{3}$$

We have introduced the discrete state energy $E_\Phi = \langle\Phi|H|\Phi\rangle$ and the discrete state-continuum coupling matrix element $M_\beta(E,\epsilon) = \langle\Phi|H-E|\chi_{\beta,\epsilon}\rangle$. The shape of the coefficient $a_\alpha(E)$ describing the dilution of the discrete state $|\Phi\rangle$ throughout a band of continuum states is obtained by solving the system (3) (for detailed derivation see Refs. [24, 25]):

$$|a_\alpha(E)|^2 = \frac{\Gamma_\alpha(E)/2\pi}{(E-E_{res})^2 + \Gamma(E)^2/4}. \tag{4}$$

This allows the interpretation of the expression

$$\Gamma(E) = \sum_{\beta=1}^{N_c}\Gamma_\beta(E) = \sum_{\beta=1}^{N_c} 2\pi|M_\beta(E,E-E_\beta)|^2 \tag{5}$$

as the (energy-dependent) resonance width. The on-shell, energy-independent quantity is obtained as $\Gamma_{loc} = \Gamma(E_{res})$, where E_{res} stands for the resonance energy

$$E_{res} = E_\Phi + \sum_{\beta=1}^{N_c} P\int \frac{|M_\beta(E,\epsilon)|^2}{E - E_\beta - \epsilon}d\epsilon. \tag{6}$$

E_{res} can often be well approximated by the discrete state energy, $E_{res} \approx E_\Phi$.

B. Algebraic diagrammatic construction of the particle-particle propagator

In order to apply the approach described above to calculation of the lifetimes of doubly ionized states the discrete state and continuum wave functions, $|\Phi\rangle$ and $|\chi_{\beta,\epsilon}\rangle$, are needed.

In the framework of many-body Green's functions techniques it is the particle-particle (pp) propagator derived from the two-particle Green's function that contains the information (excitation energies, transition moments) about doubly ionized states of an N-particle system. The pp-propagator is defined as the limit [26, 27]

$$\mathbf{\Pi}(t,t') = \lim_{\substack{t_1,t_2\to t \\ t'_1,t'_2\to t'}} i\boldsymbol{G}(t_1,t_2;t'_1,t'_2) \tag{7}$$

where the two-particle Green's function is

$$G_{rs,r's'}(t_1,t_2;t'_1,t'_2) = -\langle\Psi_0^N|\hat{T}c_r(t_1)c_s(t_2)c^\dagger_{s'}(t'_2)c^\dagger_{r'}(t'_1)|\Psi_0^N\rangle. \tag{8}$$

Here, $|\Psi_0^N\rangle$ is the exact ground state of the N-particle system, r, s label the states of a suitable one-particle basis (usually the Hartree-Fock orbitals), $c_r(t)$ denote the field operators in Heisenberg representation, and $\hat{T}$ is the Wick's time ordering operator. Assuming a time-independent Hamiltonian, the Fourier transform of the pp-propagator can be introduced,

$$\mathbf{\Pi}(\omega) = \int e^{i\omega(t-t')}\mathbf{\Pi}(t,t')d(t-t') = \mathbf{\Pi}^{\mathrm{I}}(\omega) - \mathbf{\Pi}^{\mathrm{II}}(\omega). \tag{9}$$

The two parts $\mathbf{\Pi}^{\mathrm{I}}(\omega)$ and $\mathbf{\Pi}^{\mathrm{II}}(\omega)$ are associated with the double attachment ($N+2$ particles) and double removal ($N-2$ particles) problem, respectively, and can be treated independently. In the following we will focus on $\mathbf{\Pi}^{\mathrm{II}}(\omega)$ which is relevant to doubly ionized systems.

Useful approximation for the pp-propagator was developed by Schirmer and Barth [27] using the so-called algebraic diagrammatic construction (ADC) technique. ADC [28–30] is based on a specific resummation of the perturbation series for the considered quantity and allows derivation of a set of systematic approximation schemes (ADC(n) schemes) which are complete through order n of perturbation theory (PT) and in addition contain infinite partial summations of the diagrammatic perturbation series. The starting point of the ADC approach is the observation that the exact $(N-2)$-particle part $\mathbf{\Pi}^{\mathrm{II}}(\omega)$ can be written in the general algebraic form

$$\mathbf{\Pi}^{\mathrm{II}}(\omega) = \boldsymbol{f}^\dagger(\omega\mathbf{1} - \boldsymbol{K} - \boldsymbol{C})^{-1}\boldsymbol{f} \tag{10}$$

where $\boldsymbol{C}$ is referred to as *effective interaction matrix*, $\boldsymbol{K}$ is the diagonal matrix of zeroth-order double-ionization energies, and $\boldsymbol{f}$ is the matrix of *modified transition amplitudes*. The matrices operate on the space of all $(N-2)$-particle configurations $|\phi_J^{N-2}\rangle$ obtained by the application of the physical excitation operators (c_i, $c_a^\dagger$) onto the Hartree-Fock (HF) ground

state $|\Phi_0^N\rangle$. The configurations may be classified as two-hole ($2h$; $|\Phi_{i,j}^{N-2}\rangle = c_i c_j |\Phi_0^N\rangle$), three-hole-one-particle ($3h1p$; $|\Phi_{a,i,j,k}^{N-2}\rangle = c_a^\dagger c_i c_j c_k |\Phi_0^N\rangle$) configurations, etc.

An essential feature of the ADC approximations is the fact that the size of the required explicit configuration space is limited for a given order n. For example, the zeroth and first order scheme is formulated in the space of $2h$ configurations only while both $2h$ and $3h1p$ configurations are required for the second and third order scheme. In general, at each even order $n = 2\mu$ the next higher class of configurations $[(\mu+2)h-\mu p]$ comes explicitly into play. Another notable advantage of the ADC approach is that the effective interaction matrix $\boldsymbol{C}$ is hermitian.

The explicit formulae for the effective Hamiltonian $\boldsymbol{K} + \boldsymbol{C}$ for the extended[50] second-order approximation of the pp-propagator [2p-GF/ADC(2)x] used in the present work can be found in Ref. [27]. Within this scheme the initial (discrete) and the final (continuum) states of the decay needed for the Fano theory are obtained as eigenvectors of the effective Hamiltonian expressed in configuration subspaces which will be specified below. The corresponding eigenvalues approximate the double-ionization energies. At the 2p-GF/ADC(2)x level the energies of the main ($2h$) states of the $(N-2)$-particle system are exact through the second order of PT while the energies of the satellite ($3h1p$) states are accurate through the first order. For comparison, in the usual wave function approach such as configuration interaction, in order to obtain the double-ionization energies correctly through the second order of PT the $4h2p$ configurations for the ionic states and the $2h2p$ configurations for the N-particle ground state have to be included explicitly into the expansion [27]. This demonstrates an essential property of the ADC approach: Although the explicit space of the ADC(2) equations is restricted to the ionic $2h$ and $3h1p$ configurations, both the effects of higher ionic configurations and of neutral ground state correlation are taken into account by the use of the *effective interaction matrix* $\boldsymbol{C}$. Its elements are no longer first-order expressions in the two-particle interaction but rather include higher-order terms.

C. Initial and final states of the decay process in the framework of 2p-GF/ADC(2)x

In this subsection we describe how the bound ($|\Phi\rangle$) and the continuum ($|\chi_{\beta,\epsilon}\rangle$) components of the $(N-2)$-electron wave function (1) can be expanded in terms of the $2h$ and $3h1p$

configurations spanning the configuration space of the 2p-GF/ADC(2)x scheme. The general strategy is to sort the configurations into those corresponding to the possible final states of the inter-atomic decay and those contributing to the expansion of the bound component $|\Phi\rangle$. The final states of the decay are characterized by three vacancies ("holes") and a single electron in the continuum ("particle") and the corresponding configurations are, therefore, to be found in the $3h1p$ excitation class[51]. The separation of the $3h1p$ configurations into the initial and final states expansions can be based on energy considerations, provided we have a good approximation of the discrete state energy E_Φ at hand prior to the calculation. The $3h1p$ configurations corresponding to the open decay channels originate from the $(N-3)$-electron $3h$ configurations which are lower in energy than the decaying state,

$$E^{(N-3)}_{i,j,k} = \langle \Phi^{(N-3)}_{i,j,k} | H | \Phi^{(N-3)}_{i,j,k} \rangle < E_\Phi, \quad |\Phi^{(N-3)}_{i,j,k}\rangle = c_i c_j c_k |\Phi^N_0\rangle. \tag{11}$$

Thus, it is possible to obtain the 2p-GF/ADC(2)x approximation for the bound component $|\Phi\rangle$ by restricting the configuration space to those excitations which satisfy the appropriate energy criterion (do not correspond to open channels),

$$|\Phi^{(N-2)}_J\rangle = \hat{C}_J |\Phi^N_0\rangle,$$

$$\{\hat{C}_J\} \equiv \{c_i c_j,\, i<j;\; c^\dagger_a c_i c_j c_k,\, i<j<k,\, E^{(N-3)}_{i,j,k} > E_\Phi\}. \tag{12}$$

Although the above approach leads in principle to an appropriate bound state, the need of *a priori* knowledge of the energy expectation value E_Φ as well as the energies of the $3h$ states $E^{(N-3)}_{i,j,k}$ represents a serious difficulty. The energy E_Φ is a result of the ADC calculation succeeding the configurations selection and, therefore, has to be somehow approximated at the selection stage. Moreover, the $3h$ energies as given by the Eq. (11) are only the lowest order approximations to the true triply ionized states energies. Due to those uncertainties in the involved energies, the scheme (12) can lead to a wrong selection whenever the initial state lies closely to one or more triple-ionization thresholds. Such a situation is rather common for the inter-atomic decay processes which typically lead to the production of low energy electrons.

In the present paper, with respect to the drawbacks of the aforementioned scheme, we follow an alternative strategy proposed in Ref. [1], which is based on the spatial rather than on the energetic characteristics of the $2h$ and $3h1p$ configurations. Consider a heteronuclear weakly bound cluster $A^{++}B$, where A^{++} is the initially doubly ionized subunit and B is

neutral at the beginning of the process. Let us further suppose that the considered excited state of A^{++} can decay by one of the inter-atomic decay mechanisms but cannot decay non-radiatively as long as it is isolated. Then, the final states of the inter-atomic decay will be characterized by three vacancies, one or more residing on the cluster subunit B. Consequently, in order to avoid open channels in the initial state expansion, one can restrict the $3h1p$ configurations in the 2p-GF/ADC(2)x expansion to those with all the holes residing on the cluster subunit A,

$$|\Phi_J^{(N-2)}\rangle = \hat{C}_J|\Phi_0^N\rangle,$$

$$\{\hat{C}_J\} \equiv \{c_j c_j,\, i<j;\; c_a^\dagger c_i c_j c_k,\, i<j<k,\, \varphi_{i,j,k} \in \mathrm{A}\}. \tag{13}$$

Here, $\varphi_i \in$ A stands for an occupied molecular spin-orbital of the neutral cluster localized on the subunit A. This way, the intra-atomic relaxation and correlation effects inside the subunit A are taken into account, whereas any kind of inter-atomic decay cannot be described due to the restriction imposed on the holes. When the 2p-GF/ADC(2)x Hamiltonian $\boldsymbol{K}+\boldsymbol{C}$ is diagonalized in the configuration subspace defined by Eq. (13), the bound component $|\Phi\rangle$ can be identified as the eigenvector with the largest overlap with the $2h$ configuration corresponding to the initial two vacancies.

The two approaches to the problem of selection of $3h1p$ configurations contributing to the initial state 2p-GF/ADC(2)x expansion are not exactly equivalent. The major difference is that the scheme (13) rejects all $3h1p$ configurations with one or more holes residing outside the subunit A and therefore cannot describe any inter-atomic correlation in the initial state. However, such $3h1p$ configurations are coupled to the $2h$ configuration describing the initial two vacancies on the subunit A much weaker than the configurations included by the scheme (13) and their effect on the bound component $|\Phi\rangle$ can be neglected. A more serious limitation of the spatial selection scheme is its inapplicability to symmetric systems, such as homonuclear diatomics, where the molecular orbitals are delocalized over two or more cluster subunits due to symmetry requirements (such as $\sigma_{g,u}$ orbitals in Ne_2). Adaptation of the method to symmetric systems for the case of ICD of inner-valence singly ionized states has been discussed in Ref. [31]. The problem proves to be significantly more complicated in the case of inter-atomic decay of doubly ionized clusters and will be addressed in a future publication.

Once the ADC approximation for the bound component $|\Phi\rangle$ is acquired, we need to

construct appropriate approximation of the continuum components $|\chi_{\beta,\epsilon}\rangle$ describing the possible final states of the inter-atomic decay. In the present approach this is done via a separate 2p-GF/ADC(2)x calculation in the configuration space spanned by all $3h1p$ configurations which originate from the $(N-3)$-electron $3h$ configurations with energy expectation value lower than E_Φ, supplemented by all $2h$ configurations which couple with them. Even though E_Φ is known at this point of the calculation, the above discussion regarding the uncertainties in evaluation of the condition (11) still holds due to the approximate character of the lowest-order energies $E^{(N-3)}_{i,j,k}$. However, the resulting total decay widths prove to be rather insensitive to the selection of $3h1p$ configurations included in the final states ADC. Thus, in order to improve the correlation in the continuum and convergence of the Stieltjes algorithm discussed in the following subsection, it is better to include all the configurations originating from the $3h$ states which are energetically close to E_Φ, even though they might correspond to closed channels. The fact that the Fano formalism does not require the orthogonality of the bound and the continuum components allows to include even some configurations which were already used in the bound component expansion. When the configuration space is constructed, the approximate continuum components $|\chi_{\beta,\epsilon}\rangle$ are identified as the 2p-GF/ADC(2)x eigenstates of $3h1p$ character:

$$|\chi_{\beta,\epsilon}\rangle \approx |\Psi^{3h1p}_q\rangle = \sum_J Y_{q,J}|\Phi^{(N-2)}_J\rangle, \qquad 1 - \sum_{[J]=3h1p} |Y_{q,J}|^2 \ll 1. \tag{14}$$

D. Application of the Stieltjes imaging technique to the calculation of decay widths

Despite the ability of 2p-GF/ADC(2)x to produce $3h1p$-like wave functions in the continuum region of the spectrum, there still exist major difficulties in associating the 2p-GF/ADC(2)x eigenstates with the continuum states of the Fano theory. These difficulties stem from the fact that the ADC(n) calculations, and *ab initio* quantum chemical calculations in general, are routinely performed using $\mathcal{L}^2$ bases, usually the Gaussian ones. As a result, the $\mathcal{L}^2$ and not the scattering boundary conditions are imposed and the wave functions $|\Psi^{3h1p}_q\rangle$ are not energy normalized, but rather to

$$\langle\Psi^{3h1p}_{q'}|\Psi^{3h1p}_q\rangle = \delta_{q',q}. \tag{15}$$

Moreover, the corresponding eigenenergies E_q^{3h1p} are discrete and are not expected to fulfill the energy conservation relation for the non-radiative decay, $E_q^{3h1p} = E_\Phi$. Finally, it is not possible to define rigorously to which decay channel particular state $|\Psi_q^{3h1p}\rangle$ belongs. Indeed, the scattering boundary condition corresponding to the outgoing electron of kinetic energy ϵ_β is not imposed on the $\mathcal{L}^2$ function $|\Psi_q^{3h1p}\rangle$, neither is it derived from an $(N-3)$-electron state of a well defined energy E_β.

In order to deal with the above complications, let us rewrite Eq. (5) as

$$\Gamma(E) = 2\pi \sum_{\beta=1}^{N_c} \langle \Phi | H - E | \chi_{\beta,E-E_\beta} \rangle \langle \chi_{\beta,E-E_\beta} | H - E | \Phi \rangle. \tag{16}$$

It can be noticed that the $|\chi_{\beta,E-E_\beta}\rangle$ define an N_c-dimensional space at a given energy E, in which they act as basis vectors. If the objective is the calculation of the total decay width only, one can perform an unitary transformation of the basis in this N_c-dimensional space,

$$\sum_{\beta=1}^{N_c} |\chi_{\beta,E-E_\beta}\rangle\langle\chi_{\beta,E-E_\beta}| = \sum_{\beta=1}^{N_c} |\chi'_{\beta,E-E_\beta}\rangle\langle\chi'_{\beta,E-E_\beta}|. \tag{17}$$

This shows that the $3h1p$ states $|\Psi_q^{3h1p}\rangle$ can be used in the calculation of the total decay widths, even though they do not correspond directly to the open decay channels. Rigorous calculations of the partial decay widths, on the contrary, are not possible in the same manner.

The use of the $\mathcal{L}^2$ 2p-GF/ADC(2)x eigenstates instead of the true continuum functions in the formula (16) can be further justified in the following way. Eq. (16) relates the total decay width to the matrix elements coupling the bound and the continuum components of the wave function, $\langle \Phi | H - E | \chi_{\beta,E-E_\beta} \rangle$. The bound component $|\Phi\rangle$ is effectively zero outside some spatial region which we will call here the "interaction region". The interaction region roughly defines the dimension of the system in which the decay process occurs and is spanned by the $\mathcal{L}^2$ basis used in the expansion of $|\Phi\rangle$. The continuum components $|\chi_{\beta,\epsilon}\rangle$ are, on the other hand, nonzero even at the infinite distance from the cluster. Apparently, the Hamiltonian matrix elements between the discrete and continuum components gain a non-vanishing contribution only from the interaction region. One can, thus, substitute the continuum components in Eq. (16) by the approximate wave functions $|\tilde{\chi}_{\beta,\epsilon}\rangle$, which are equivalent to the true continuum components within the interaction region and go to zero outside. Consequently, it is possible to use $\mathcal{L}^2$ approximations, such as $|\Psi_q^{3h1p}\rangle$, in the total width calculation, provided they are

1. re-normalized such that they are equal to the continuum wave functions inside the interaction region,

2. interpolated in energy such that they satisfy the energy conservation $E_q^{3h1p} = E_\Phi$.

Both these goals can be achieved using the procedure known as the Stieltjes imaging. This technique has been introduced by Langhoff [32] in the context of the calculation of the photoionization cross section using the $\mathcal{L}^2$ wave functions and generalized to evaluate decay rates evaluation by Hazi [33]. The renormalization of the so-called pseudo-spectrum of the discrete $\mathcal{L}^2$ states possessing energies in the continuum region of the true spectrum can be achieved using the fact that the spectral moments of the quantities of the type of Eq. (5) calculated using the pseudo-spectrum are good approximations to the spectral moments constructed using the true continuum. In our case this leads to

$$\sum_\beta \int E^k |\langle \Phi | H - E | \chi_{\beta, E-E_\beta} \rangle|^2 dE \approx \sum_q (E_q^{3h1p})^k \langle \Phi | H - E | \Psi_q^{3h1p} \rangle|^2. \tag{18}$$

This property allows us to use the techniques of the moment theory in order to obtain the correct matrix element of the kind of Eq. (5) interpolated to the needed value of the continuum state energy [i.e., $E_{res} \approx E_\Phi$, cf. Eq. (6)]. This can be done through a series of consecutive approximations of increasing order n_S. At each order the renormalized decay width is obtained in terms of quadrature abscissas and weights for a generalized Gaussian quadrature rule associated with the weight function $\Gamma(E)$. n_S is the order of the highest orthogonal polynomial generated during the Stieltjes imaging calculation which is equivalent to the use of the lowest $2n_S - 1$ approximate spectral moments (18). For details of the implementation of the method employed in the present work, see Refs. [34, 35]. The more spectral moments one can reliably calculate using the pseudo-spectrum the higher is the maximal possible value of n_S and also the quality of the final result. A reliable calculation of the spectral moments, in turn, requires a high density of the pseudo-spectrum states. The density can be controlled by the choice of the $\mathcal{L}^2$ basis.

As noted above, the necessity of the transformation (17) prevents the formulation of a rigorous procedure for the calculation of the partial widths within the framework of the present method. Such a calculation must involve the true degenerate continuum functions corresponding to the various decay channels, which is not the case for the $\mathcal{L}^2$ states $|\Psi_q^{3h1p}\rangle$.

Nevertheless, it is still possible to estimate partial widths using the Stieltjes imaging technique by an *ad hoc* procedure suggested in Refs. [1, 36]. It can be summarized as follows:

1. For each $3h$ channel β, construct the channel-specific couplings,

$$\gamma_{q,\beta}(E) = 2\pi|\langle\Psi|H - E|\hat{P}_\beta\Psi_q^{3h1p}\rangle|^2, \tag{19}$$

   where $\hat{P}_\beta$ is the projection operator corresponding to the given channel.

2. Apply the Stieltjes imaging procedure to the couplings $\gamma_{q,\beta}(E)$ using the corresponding energies E_q^{3h1p} in order to obtain the un-normalized estimates for the partial rates $\tilde{\Gamma}_\beta$ at the energy E_Φ.

3. Normalize the obtained estimates such that they sum up to the correct total rate Γ:

$$\Gamma_\beta \approx \frac{\tilde{\Gamma}_\beta}{\sum_\beta \tilde{\Gamma}_\beta}\Gamma. \tag{20}$$

Within the 2p-GF/ADC(2)x approach the projection operators $\hat{P}_\beta$ are defined naturally since each $3h1p$ configuration corresponds to three specific holes defining (together with the spin state) in the lowest-order approximation one of the final states of the decay. Thus, we put

$$\hat{P}_\beta = \sum_a |\tilde{\Phi}^{N-2}_{a,i,j,k,\xi}\rangle\langle\tilde{\Phi}^{N-2}_{a,i,j,k,\xi}|, \tag{21}$$

where the wave functions $|\tilde{\Phi}^{N-2}_{a,i,j,k,\xi}\rangle$ differ from the $3h1p$ configurations $|\Phi^{N-2}_{a,i,j,k}\rangle$ in that they are spin-adapted, i.e., their spin parts are eigenfunctions of the total spin operators for both the $(N-2)$- and $(N-3)$-electron systems. Therefore, the channel index β is in one to one correspondence with the combination of the hole indices i, j, k and the $3h1p$ spin state ξ. Such a choice of the projection operators is expected to produce reasonable results whenever the inter-channel coupling is weak, such as between the ETMD and ICD classes of channels (i.e., between the final states of the types A^+B^{++} and $A^{++}B^+$ respectively). Within each of the ICD or ETMD classes, on the other hand, the inter-channel coupling can be strong and any partial width obtained via the above approach has to be considered as a crude approximation only.

III. ICD AFTER AUGER IN VAN DER WAALS CLUSTERS

Two classes of systems exhibiting inter-atomic decay, which have been studied intensively in the past, are rare-gas and alkaline-earth-rare-gas clusters. ICD following single inner-valence ionization of Ne in neon-rare-gas clusters were investigated theoretically and experimentally in a series of works [4, 5, 31, 37–39]. The alkaline-earth-rare-gas clusters were studied by Averbukh and co-workers in Refs. [1, 40]. Inter-atomic decay following Auger decay in clusters, predicted in Ref. [7], was first observed experimentally in argon dimers [12] and in ArKr [13] and more recently in neon dimers [14–16]. The potential energy curves of all the states involved in the cascades of the Ar and Ne dimers have been reported by Stoychev *et al.* [41, 42]. Except of the single-point computation in Ref. [7] nothing is known on the respective ICD rates. It is thus natural to apply the present method first to diatomic rare-gas clusters. We will also pay attention to alkaline-earth-rare-gas clusters as they exhibit considerably different behavior. In the following we report on the results of the calculations on the ICD widths of $Ne^{2+}(2s^{-1}2p^{-1})Ar$ and $MgNe^{2+}(2s^{-1}2p^{-1})$.

However, before we move on to the application of the presented method to the calculation of the inter-atomic decay widths of doubly ionized clusters, it is desirable to perform benchmark calculations on a system with known decay width. Since essentially nothing is known about the inter-atomic decay widths of doubly ionized clusters we had to look for a suitable atomic Auger decay process. By far the most extensively studied is the decay of multiply-ionized neon with the $1s$ vacancy. The major disadvantage of this system is that it produces fast Auger electrons with kinetic energy over 800 eV. Such electrons are very difficult to describe using Gaussian basis sets. Nevertheless, despite rather low density of the pseudo-spectrum $|\Psi_q^{3h1p}\rangle$ at the desired energy, the Stieltjes algorithm converges and stable results with respect to basis set can be obtained.

We have used the standard cc-pV6Z basis for Ne augmented by additional [5s,5p,5d] Gaussian functions on Ne and [3s,3p,3d] functions on 6 ghost centers around the atom. In Tab. I the present results are compared to the recent calculation by Karim and Logan [43], who used the self-consistent Hartree-Fock model with the inclusion of the spin-orbit coupling. Good agreement of their data with the older work by Bhalla *et al.* [44] shows that the effects arising from the spin-orbit coupling are negligible and therefore the present theory should be adequate for the description of the process under consideration. We observe that the present

method produces decay widths which are by 10-20% smaller than those calculated by Karim and Logan. Considering the difficulties stemming from the high kinetic energies of the Auger electrons and also the imperfections of the reference calculations the agreement is very good. Besides this comparison, the reliability of the present method is further supported by the success of the original Fano-ADC-Stieltjes method based on 1p-GF/ADC(2x), which has been tested extensively for both intra- and inter-atomic decay processes of singly ionized and excited states [1, 31].

A. Rare-gas clusters

Let us proceed to the study of inter-atomic decay in NeAr dimer. The calculations of the decay widths have been carried out using cc-pVTZ bases on both Ne and Ar atoms augmented by continuum-like diffuse functions of the Kaufmann-Baumeister-Jungen (KJB)-type [45], $5s5p5d$ on Ne, $6s6p8d3f$ on Ar, and by additional $3s3p3d$ KJB-type functions at the centers $(0,0,0)$, $(0,0,\pm R/4)$ and $(0,0,\pm 5R/8)$. Here, R is the internuclear distance and the molecular axis is along the z-axis. With this choice we achieved good convergence in the basis as well as reliable Stieltjes imaging results.

Fig. 1 shows the energies of all considered levels of triply ionized NeAr together with the potential energies of the initial states of the decay, $\mathrm{Ne}^{2+}(2s^{-1}2p^{-1}\ {}^1P)\mathrm{Ar}$ (red) and $\mathrm{Ne}^{2+}(2s^{-1}2p^{-1}\ {}^3P)\mathrm{Ar}$ (blue). The latter curves are the Fano discrete state energies obtained by 2p-GF/ADC(2)x in a restricted set of configurations as described in Sec. II C, and shifted to match the known atomic data at large inter-atomic distances R. The fact that in ICD after Auger there are two possible spin multiplicities of the initial state is one of the main differences compared to ICD of a single inner-valence vacancy and we will see that it brings about some interesting phenomena. Furthermore, the initial state can exhibit either Σ or Π spatial symmetry. The Σ symmetry is (at large internuclear distances) characterized by the $\mathrm{Ne}(2p_z)$ vacancy while the Π symmetry by the $\mathrm{Ne}(2p_x)$ or $\mathrm{Ne}(2p_y)$ one. The corresponding energies differ only a little below the equilibrium internuclear distance R_{eq} of the neutral cluster and are degenerate at large internuclear distances. Therefore, the two red and two blue curves are nearly indistinguishable in the scale of Fig. 1.

The black, brown and green curves represent the three classes of accessible final states of the decay, see below. The corresponding energies have been calculated in the lowest-

order approximation of Eq. (11) and again shifted to match atomic values at large R. The black curves represent the final states of ICD, $\mathrm{Ne}^{2+}(2p^{-2})\mathrm{Ar}^{+}(3p^{-1})$. This class splits into three groups approaching different energies in the asymptotic range, characterized by the symmetry of the doubly ionized neon. The highest-lying group contains doublet $3h$ states $\mathrm{Ne}^{2+}(2p^{-2}\ {}^1S)\mathrm{Ar}^{+}(3p^{-1})$, the middle one doublet states $\mathrm{Ne}^{2+}(2p^{-2}\ {}^1D)\mathrm{Ar}^{+}(3p^{-1})$, and the lowest group comprises both the doublet and quartet $3h$ states $\mathrm{Ne}^{2+}(2p^{-2}\ {}^3P)\mathrm{Ar}^{+}(3p^{-1})$. The brown curves are the energies of the final states of ETMD, $\mathrm{Ne}^{+}(2p^{-1})\mathrm{Ar}^{2+}(3p^{-2})$, again splitting into three groups according the ${}^1S$, ${}^1D$ and ${}^3P$ symmetry of Ar^{2+}. The last class of final states (green curves) are the ETMD channels $\mathrm{Ne}^{+}(2p^{-1})\mathrm{Ar}^{2+}(3s^{-1}3p^{-1})$. The higher-lying states correspond to ${}^1P$ while the lower lying to ${}^3P$ symmetry of Ar^{2+}.

Fig. 2 shows the total decay widths of the doubly ionized singlet ${}^1\Sigma$ ($\Gamma^{{}^1\Sigma}$, dashed line) and ${}^1\Pi$ ($\Gamma^{{}^1\Pi}$, dash-dotted line) states of $\mathrm{Ne}^{2+}(2s^{-1}2p^{-1})\mathrm{Ar}$. As a reference, the total decay width Γ^{2s} of the single vacancy $\mathrm{Ne}^{+}(2s^{-1})\mathrm{Ar}$ calculated by the method of Ref. [1] (equivalent to the present one) is shown by the full line. The fast decreasing curves in the lower left corner are the partial ETMD widths. The first observation is that the decay width of both the singly and doubly ionized initial states follow quite closely the $1/R^6$ dependence (dotted line), predicted for dipole-allowed inter-atomic decay processes at large interatomic distances (cf *virtual photon transfer model*, [21, 40, 46]), over the whole geometry range. At the equilibrium geometry, $\Gamma^{{}^1\Sigma}$ is about twice larger than Γ^{2s}, while $\Gamma^{{}^1\Pi}$ is only about 1.3 times larger. The ETMD partial widths $\Gamma^{{}^1\Sigma}_{ETMD}$ and $\Gamma^{{}^1\Pi}_{ETMD}$ behave also quite similarly to Γ^{2s}_{ETMD}, but the ratio of the magnitudes is slightly larger than found for the respective ICD widths (about 2.5 for both symmetries). As expected, all ETMD partial widths decrease exponentially with increasing R which is caused by the electron-transfer character of the process which requires overlap of the wave functions of the involved atoms.

The similar qualitative behavior of the widths of singly and doubly ionized initial states with the same inner-valence vacancy can be understood by looking at the decay process in the first order of PT. Fig. 3 shows the two possible pathways of the inter-atomic decay – the energy transfer and the electron transfer (cf Eqs. (1)–(5) in Ref. [7]). The important point is that in the first order of PT the initial $2p$ vacancy on Ne is only a spectator. Therefore, the whole picture is very similar to that of ICD of a single $2s$ vacancy. The present method goes beyond first order PT and accounts also for the higher-order processes involving pathways in which the initial $2p$ vacancy participates actively. The analysis of the

partial widths (cf Sec. II D) shows, however, that the contribution of those processes is only up to 5% of the total width. The difference in magnitude of the decay widths of singly and doubly ionized states is, therefore, to be attributed to the fact that the spectator $2p$ vacancy changes substantially the symmetry of the decaying state and the shape of the occupied orbitals. Another interesting effect of the spectator $2p$ vacancy is that the $^1\Sigma$ state decays faster than the $^1\Pi$ state, even though the leading contribution to the decay width comes in both cases from the same integral $(\varphi_{\mathrm{Ne}(2s)}\varphi_{\mathrm{Ne}(2p_z)}|\mathbf{k}\varphi_{\mathrm{Ar}(3p_z)})$, at least at large internuclear distances where the notation φ_i for spatial atomic orbitals notation is meaningful (see also the discussion concerning partial decay widths). The presence of Ne($2p$) vacancy parallel (Σ) or perpendicular (Π) to the molecular axis changes in a different ways the shape of the occupied atomic orbitals, leading to variations of the magnitude of the inter-atomic decay widths.

Fig. 4 shows the total decay width of the triplet states of $\mathrm{Ne}^{2+}(2s^{-1}2p^{-1})\mathrm{Ar}$. Again, dashed and dash-dotted lines correspond to $^3\Sigma$ and $^3\Pi$ symmetries, respectively. The full line shows the reference Γ^{2s} of the single vacancy $\mathrm{Ne}^{+}(2s^{-1})\mathrm{Ar}$ which is, of course, the same as in Fig. 2. The most striking difference between the decaying states of triplet and singlet multiplicity is the substantial change in the magnitude of their total decay widths. While in the singlet multiplicity the decay widths of the doubly ionized states in both Σ and Π symmetries are larger than that of a single $2s$ vacancy, the contrary is true for the triplet multiplicity where both $\Gamma^{^3\Sigma}$ and $\Gamma^{^3\Pi}$ drop below Γ^{2s}. This decrease is stronger in the case of Σ symmetry, to the extent that the $^3\Sigma$ state decays slower than the $^3\Pi$ state although in the singlet spin multiplicity the opposite applies.

In order to explain this interesting behavior we have to analyze the partial widths for the ICD process. Even though we emphasized in Sec. II D that the proposed method to compute partial widths is non-rigorous, we believe that the obtained qualitative picture is correct. In Tab. II we have summarized partial ICD decay widths into three distinct classes of the $3h$ channels defined by their total spin multiplicity and the symmetry of the Ne^{2+} dication. The first column describes the symmetry of the initial doubly ionized state $\mathrm{Ne}^{2+}(2s^{-1}2p^{-1})\mathrm{Ar}$. The second column lists the partial widths into the doublet $3h$ channels derived from the singlet $\mathrm{Ne}^{2+}(2p^{-2}\ ^1S/D)$ (i.e., we have summed partial decay widths for all doublet channels characterized by the singlet $\mathrm{Ne}^{2+}(2p^{-2}\ ^1S/D)$ and arbitrary $3p$ hole on Ar), third column those into the doublet channels derived from the triplet $\mathrm{Ne}^{2+}(2p^{-2}\ ^3P)$,

and the fourth column those into the quartet $3h$ channels. Quartet final states are accessible only from the triplet initial states. The last two columns list the total decay widths and ICD lifetimes, respectively. We observe that the singlet initial states decay almost exclusively into doublet $Ne^{2+}(2p^{-2}\ ^1S/D)Ar^+(3p^{-1})$ states, the $^1\Sigma$ state decaying thereby 1.5 faster than the $^1\Pi$ state. In the case of triplet initial states, the efficiency of the decay into the same final doublet states drops by a factor of about 10 (even more in the case of $^1\Sigma$ initial state). Now, however, the quartet channels are accessible and become the most efficiently populated. The contribution of the doublet channels with $Ne^{2+}(2p^{-2}\ ^3P)$ is negligible for all initial states.

The question we would like to answer is: why does the $^3\Pi$ state decay faster than the $^3\Sigma$ one although the opposite situation is encountered in the singlet multiplicity. In the following discussion we show how the $Ne(2p_z)$ vacancy in the $^3\Sigma$ decaying state hinders some of the decay pathways which are among the most efficient ones for the other considered initial states.

It is not surprising that the most efficient decay processes are those which proceed via energy-transfer where the involved orbitals are spatially as close to each other as possible. Speaking in terms of atomic orbitals, the most efficient pathway would be where an electron from the $Ne(2p_z)$ orbital fills the $Ne(2s)$ vacancy and another electron is ejected from the $Ar(3p_z)$ orbital, whenever this pathway is operative. In the following we will refer to it as the *main ICD pathway*. In the $^1\Pi$ decaying state the initial outer-valence vacancy is either $Ne(2p_x)$ or $Ne(2p_y)$ and the $Ne(2p_z)$ orbital is doubly occupied. Therefore, an electron with the spin appropriate to fill the $Ne(2s)$ vacancy is available and the main ICD pathway leads to the doublet $Ne^{2+}(2p_{x,y}^{-1}2p_z^{-1}\ ^1D)Ar^+(3p_z^{-1})$ final state. In the $^1\Sigma$ decaying state the $Ne(2p_z)$ orbital is only singly occupied but the remaining electron has the opposite spin than the one left in the $Ne(2s)$ orbital. Hence, the main ICD pathway is again operative and results in the doublet $Ne^{2+}(2p_z^{-2}\ ^1S/D)Ar^+(3p_z^{-1})$ state. Corresponding partial widths are plotted as the full lines in the upper ($^1\Sigma$) and lower ($^1\Pi$) panel of Fig. 5, respectively. For both the $^1\Pi$ and $^1\Sigma$ decaying states the above discussed partial widths are found to be the largest indeed.

The situation becomes more involved for the triplet decaying states. The cause of the substantial decrease of the partial widths into the doublet $Ne^{2+}(^1S/D)Ar^+$ channels lies in the fact that an atom cannot change the total spin during an intra-atomic radiative

decay. Therefore, in the first order of PT, the final states involving $Ne^{2+}(^1S/D)$ are only accessible via an electron-transfer processes where the Ne($2s$) vacancy is filled by an Ar($3p$) electron with successive ejection of an electron from the Ne($2p$) orbital. Still, energy-transfer pathways can be found in the second order of PT. In Fig. 5 the dashed lines show the largest partial widths into the doublet $Ne^{2+}(^1S/D)Ar^+$ final states for the $^3\Sigma$ (upper panel) and $^3\Pi$ (lower panel) decaying states. We observe that the higher-order contributions prevail and the partial widths exhibit the $1/R^6$ dependence on the internuclear distance.

Let us turn our attention to the quartet $Ne^{2+}(^3P)Ar^+$ channels and consider again the main ICD pathway. The analysis of the $^3\Pi$ initial state is fully analogical to that of the $^1\Pi$ one. The Ne($2p_z$) orbital is doubly occupied and, therefore, one of the electrons can drop into the Ne($2s$) vacancy, leading via the main ICD pathway to the quartet $Ne^{2+}(2p_{x,y}^{-1}2p_z^{-1})Ar^+(3p_z^{-1})$. Corresponding partial width is plotted as the dashed-dotted line in the lower panel of Fig. 5. Comparison with other partial widths confirms that the main ICD pathway is the most efficient decay process. In the case of the $^3\Sigma$ decaying state the initial outer-valence vacancy is Ne($2p_z$). The fact that this orbital which plays an important role in the main ICD pathway is only singly occupied changes the situation considerably. If the main ICD pathway were operative, the final state would be quartet $Ne^{2+}(2p_z^{-2}\ ^3P)Ar^+(3p_z^{-1})$ but such a state does not exist. In other words, the main ICD pathway is hindered by the initial Ne($2p_z$) vacancy since the single electron left in this orbital has incorrect spin to fill the Ne($2s$) hole. Therefore, in the case of $^3\Sigma$ decaying state the inner-valence vacancy can only be refilled by an electron from the Ne($2p_x$) or Ne($2p_y$) orbitals. This, however, leads to less efficient transfer of the excess energy to the neighboring argon. Corresponding partial width, shown by the dashed-dotted line in the upper panel of Fig. 5, is about 3.5 times smaller than the partial width of the main ICD pathway for the $^3\Pi$ decaying state. It should be noted that also in the case of the $^3\Pi$ state the initial outer-valence hole blocks certain decay pathways, but only the less efficient ones. Therefore, the total ICD width $\Gamma^{^3\Pi}$ is larger than $\Gamma^{^3\Sigma}$.

B. Alkaline-earth-rare-gas clusters

After the thorough discussion on $Ne^{2+}Ar$ let us report now more briefly on ICD in $MgNe^{2+}$. The calculations have been carried out using uncontracted cc-pVQZ basis sets

on both atoms augmented by $9s9p9d$ KJB-type diffuse functions on Ne, $6s6p6d$ functions on Mg and $5s5p5d$ functions at the centers $(0,0,0)$, $(0,0,\pm R/4)$ and $(0,0,\pm 5R/8)$. The potential energy curves of the doubly and triply ionized states involved in the decay calculated on the same level of theory as in the case of NeAr are plotted in Fig. 6. Note that there are three more open ETMD channels of the type $Mg^{2+}(3s^{-2})Ne^{+}(2p^{-1})$. These lie at rather low energy in the range 46–54 eV and are not shown in the figure. Included in the figure are the higher-lying ETMD channels $Mg^{2+}(2p^{-1}3s^{-1})Ne^{+}(2p^{-1})$ to demonstrate that they are closed over the whole range of internuclear distances.

Figs. 7 and 8 show the ICD and ETMD widths of the singlet and triplet states of $MgNe^{2+}(2s^{-1}2p^{-1})$, respectively. The full line represents in both figures the reference ICD width of $MgNe^{+}(2s^{-1})$. We observe that, as in the case of NeAr, the ICD and ETMD widths of doubly ionized states behave qualitatively as those of the single inner-valence vacancy. However, in strong contrast to NeAr the decay widths of MgNe follow the virtual photon transfer model behavior $1/R^6$ only at very large internuclear distances, $R > 9$ Å. At smaller internuclear distances pronounced orbital overlap enhancement of the ICD widths is evident. The magnitude of the non-radiative decay widths, though, is significantly smaller than in the case of NeAr at the respective equilibrium internuclear distances [compare the lifetime 1300 fs of $MgNe^{+}(2s^{-1})$ and 48 fs of $Ne^{+}(2s^{-1})Ar$]. This cannot be explained solely by the reduced number of decay channels, stemming from the fact that there are six electrons in the $Ar(3p)$ shell but only two in the $Mg(3s)$ shell. The deeper reason for the increased lifetime of $MgNe^{+}(2s^{-1})$ can be understood in terms of the so called *virtual photon transfer model* [46] which relates the interatomic decay width to the radiative lifetime of the initial vacancy and the total photoionization cross section of the secondarily-ionized atom. At the virtual photon energy $E[Ne^{+}(2s^{-1}\ ^2S)] - E[Ne^{+}(2p^{-1}\ ^2P)]$ the photoionization cross section of Mg is $\sigma_{Mg} = 0.26$ Mb which is very small compared to that of Ar, $\sigma_{Ar} = 31$ Mb [47]. The connection of the decay rates and ionization cross sections and other quantities in the context of ICD was discussed at length by Averbukh *et al.* [40]. At this point it is also interesting to assess the strong effect of the orbital overlap observed in MgNe by comparing the decay rates of $Ne^{+}(2s^{-1})Ar$ and $MgNe^{+}(2s^{-1})$ at the equilibrium distance of NeAr ($R_{eq} = 3.5$ Å). At that distance the rates become rather comparable, reaching the values of $\Gamma^{2s} = 13.6$ meV for $Ne^{+}(2s^{-1})Ar$ and $\Gamma^{2s} = 3.3$ meV for $MgNe^{+}(2s^{-1})$, respectively. Clearly, the much larger equilibrium distance of MgNe is a central factor. Because of that nuclear dynamics is ex-

pected to play an important role for MgNe. Once the nuclear wave packet is created on the attractive potential curves of $MgNe^{2+}(2s^{-1}2p^{-1})$, it will move towards smaller internuclear distances where the decay is strongly enhanced.

The significant orbital overlap enhancement of the decay rates indicates that electron-transfer processes strongly influence the inter-atomic decay at small internuclear distances. This also shows up in the dependence of the rates on the spin multiplicity and symmetry of the decaying state. For example, in NeAr we observed that the decay processes $Ne^{2+}(2s^{-1}2p^{-1}\ {}^3P)Ar \rightarrow Ne^{2+}(2p^{-1}\ {}^1S/D)Ar^{+}(3p^{-1})$ were strongly suppressed. As explained in the previous subsection, the reason lies in the fact that those processes are essentially of electron-transfer character due to the necessity for the change of the total spin of the Ne^{2+} cation (energy-transfer pathways can only be found in higher orders of PT). Since in the case of MgNe the electron transfer prevails over the energy transfer the doublet states $Mg^{+}(3s^{-1})Ne^{2+}(2p^{-1}\ {}^1S/D)$ are nearly equally populated in both $^1\Pi$ and $^3\Pi$ symmetries, see the second column in Tab. III. For the same reason we observe from Fig. 8 that the decay of $MgNe^{2+}(2s^{-1}2p^{-1})$ is similarly efficient in $^3\Sigma$ and $^3\Pi$ symmetries below $R = 5\,\text{Å}$. The decay width of the $^3\Sigma$ state significantly decreases due to the effects discussed in the context of NeAr at larger internuclear distances where energy transfer starts to dominate.

IV. CONCLUSIONS

In the present paper we have presented an $\mathcal{L}^2$ method for the calculation of the total widths of inter-atomic (inter-molecular) decay processes of excited doubly ionized states of clusters. Thereby, we focus mainly on those doubly ionized states which are the final states of the common Auger decay of core levels. The approach is fully analogous to that of Ref. [1] developed for the calculation of the total rates of the inter-atomic decay of singly ionized clusters. Both methods are based on the Fano resonance formalism, the ADC approach to the solution of the multi-electron problem, and the Stieltjes imaging technique for the renormalization of the discretized continuum. The fundamental difference between the two methods is that the present one is based on the two-particle propagator in order to describe doubly ionized intermediate states and triply ionized final states of the decay plus an electron in continuum. In the present implementation, based on the 2p-GF/ADC(2)x scheme, the former states are treated correctly through the second order of perturbation theory while the

latter ones are exact through the first order. The method takes into account physical effects like intra-atomic correlation and orbital relaxation in the initial state and inter-channel mixing in the final states of the decay. In principle, the method can be further improved by making use of higher ADC approximations. ADC(3) level of theory [30], improving significantly the description of the initial state, would still be computationally tractable as it does not increase the configuration space. The ADC(4) level, necessary to further improve the description of the final states of the decay, introduces the next higher $4h2p$ excitation class and would significantly increase the computational demands.

One of the most notable advantages of the ADC-based approach is the separability of the ADC solution of the multi-electron problem with respect to dissociation of the system into non-interacting fragments (size-consistency). The method is therefore expected to be able to treat also polyatomic and molecular clusters. However, possible violation of the charge-consistency in the ADC expansion of the pp-propagator has to be carefully analized whenever the method is to be applied to extended systems as it can lead into improper scaling of the physical properties with increasing size of the system [23]. Another important feature of the presented method is the ability of the Stieltjes imaging technique to produce converged results of the ICD and ETMD decay widths over six or more orders of magnitude (cf Fig. 5). Such an accuracy is essential for precise description of the inter-atomic decay processes. One of the most serious drawbacks of the method is connected with the selection of the physical excitation operators in the bound-state calculation. The implemented approach [see Sec. II C] can become ambiguous for clusters with significant orbital overlap, such as hydrogen-bonded clusters, and is completely inapplicable to systems with molecular orbitals delocalized due to the inversion symmetry. For such systems specific selection schemes have to be developed. Another limitation of the present approach is its inability to produce accurate partial decay widths, which is caused by the $\mathcal{L}^2$ description of the decay continuum. We have shown, however, that the non-rigorous procedure of Ref. [36] for the estimation of partial decay widths can give many very interesting answers at least at the semi-qualitative level.

In the present paper the methodology was applied to study the decay rates of different $Ne^{2+}(2s^{-1}2p^{-1})$ states in NeAr and MgNe. It has been shown that the presence of a spectator Ne $2p$-hole does not influence much the dependence of the decay width on the internuclear distance found in the decay of a single $Ne(2s^{-1})$ vacancy. On the other hand,

the magnitude of the decay width depends on the symmetry and spin multiplicity of the decaying doubly ionized states. Partial widths analysis was used successfully to explain these effects. Pronounced differences between NeAr and MgNe clusters are found. They are caused in part by the small photoionization cross section of Mg, which allows the contribution of electron-transfer decay pathways to be revealed. The shortest lifetimes are found for the $Ne^{2+}(2s^{-1}2p^{-1})Ar$ and the $MgNe^{2+}(2s^{-1}2p^{-1})$ state of the $^1\Sigma$ symmetry. These lifetimes are 25 fs and 833 fs, respectively, at the respective equilibrium geometry. If MgNe had the same internuclear distance as NeAr, its lifetime would have been 145 fs. Finally, we remark that in larger clusters the lifetimes are much shorter due to the increased number of neighbors. Furthermore, as shown by Deleuze and co-workers [48], ICD in larger van der Waals molecular clusters need not necessarily lead to Coulombic explosion but can also initiate rather complex charge rearrangement reactions resulting in the formation of covalently bound dicationic assemblies. These remarkable features makes the polyatomic systems interesting objects to study.

Acknowledgments

We would like to thank V. Vysotskiy for help with implementation of the *ab initio* code. P. K. would like to acknowledge the financial support by the Alexander von Humboldt Foundation and by the Center of Theoretical Astrophysics No. LC06014 of the Ministry of Education, Youth and Sports of the Czech Republic. V. A. acknowledges the financial support of the Max Planck Society through the Distinguished PKS Postdoctoral Fellowship. Financial support by the DFG is acknowledged.

[1] V. Averbukh and L. S. Cederbaum, J. Chem. Phys. **123**, 204107 (2005).

[2] L. S. Cederbaum, J. Zobeley, and F. Tarantelli, Phys. Rev. Lett. **79**, 4778 (1997).

[3] S. Marburger, O. Kugeler, and U. Hergenhahn, Phys. Rev. Lett. **90**, 203401 (2003).

[4] T. Jahnke, A. Czasch, M. S. Schöffler, S. Schössler, A. Knapp, M. Käsz, J. Titze, C. Wimmer, K. Kreidi, R. E. Grisenti, et al., Phys. Rev. Lett. **93**, 163401 (2004).

[5] J. Zobeley, R. Santra, and L. S. Cederbaum, J. Chem. Phys. **115**, 5076 (2001).

[6] E. Rühl, A. Knop, A. P. Hitchcock, P. A. Dowben, and D. N. McIlroy, Surf. Rev. Lett. **3**, 557 (1996).

[7] R. Santra and L. S. Cederbaum, Phys. Rev. Lett. **90**, 153401 (2003).

[8] H. P. Kelly, Phys. Rev. A **11**, 556 (1975).

[9] W. Mehlhorn, D. Stalherm, and H. Verbeek, Z. Naturforsch. **A 23**, 287 (1968).

[10] I. Kádár, S. Ricz, J. Végh, B. Sulik, D. Varga, and D. Berényi, Phys. Rev. A **41**, 3518 (1990).

[11] T. Sommerfeld, U. V. Riss, H.-D. Meyer, L. S. Cederbaum, B. Engels, and H. U. Suter, J. Phys. B **31**, 4107 (1998).

[12] Y. Morishita, X.-J. Liu, N. Saito, T. Lischke, M. Kato, G. Prümper, M. Oura, H. Yamaoka, Y. Tamenori, I. H. Suzuki, et al., Phys. Rev. Lett. **96**, 243402 (2006).

[13] Y. Morishita, N. Saito, I. H. Suzuki, H. Fukuzawa, X.-J. Liu, K. Sakai, G. Prümper, K. Ueda, H. Iwayama, K. Nagaya, et al., J. Phys. B **41**, 025101 (2008).

[14] K. Kreidi, T. Jahnke, T. Weber, T. Havermeier, R. E. Grisenti, X. Liu, Y. Morisita, S. Schössler, L. P. H. Schmidt, M. Schöffler, et al., J. Phys. B **41**, 101002 (2008).

[15] K. Kreidi et al., to be published.

[16] M. Yamazaki, J. Adachi, Y. Kimura, A. Yagishita, M. Stener, P. Decleva, N. Kosugi, H. Iwayama, K. Nagaya, and M. Yao, Phys. Rev. Lett. **101**, 043004 (2008).

[17] R. Santra, J. Zobeley, and L. S. Cederbaum, Phys. Rev. B **64**, 245104 (2001).

[18] F. Mertins and J. Schirmer, Phys. Rev. A **53**, 2140 (1996).

[19] F. Mertins, J. Schirmer, and A. Tarantelli, Phys. Rev. A **53**, 2153 (1996).

[20] R. Santra and L. S. Cederbaum, J. Chem. Phys. **115**, 6853 (2001).

[21] R. Santra and L. S. Cederbaum, Phys. Rep. **368**, 1 (2002).

[22] M. S. Deleuze, M. K. Scheller, and L. S. Cederbaum, J. Chem. Phys. **103**, 3578 (1995).

[23] M. S. Deleuze, Int. J. Quant. Chem. **93**, 191 (2003).

[24] U. Fano, Phys. Rev. **124**, 1866 (1961).

[25] G. Howat, T. Åberg, and O. Goscinski, J. Phys. B **11**, 1575 (1978).

[26] N. Fukuda, F. Iwamoto, and K. Sawada, Phys. Rev. **135**, A932 (1964).

[27] J. Schirmer and A. Barth, Z. Phys. A **317**, 267 (1984).

[28] J. Schirmer, Phys. Rev. A **26**, 2395 (1982).

[29] J. Schirmer, L. S. Cederbaum, and O. Walter, Phys. Rev. A **28**, 1237 (1983).

[30] A. Tarantelli and L. S. Cederbaum, Phys. Rev. A **39**, 1639 (1989).

[31] V. Averbukh and L. S. Cederbaum, J. Chem. Phys. **125**, 094107 (2006).

[32] P. W. Langhoff, in *Electron-Molecule and Photon-Molecule Collisions*, edited by T. Rescigno, V. McKoy, and B. Schenider (Plenum, New York, 1979).

[33] A. U. Hazi, in *Electron-Molecule and Photon-Molecule Collisions*, edited by T. Rescigno, V. McKoy, and B. Schenider (Plenum, New York, 1979).

[34] F. Müller-Plathe and G. H. F. Diercksen, Phys. Rev. A **40**, 696 (1989).

[35] F. Müller-Plathe and G. H. F. Diercksen, in *Electronic Structure of Atoms, Molecules and Solids*, edited by S. Canuto, J. D'Albuquerque e Castro, and F. J. Paixão (1990).

[36] I. Cacelli, V. Caravetta, and R. Moccia, Mol. Phys. **59**, 385 (1986).

[37] R. Santra, J. Zobeley, and L. S. Cederbaum, Phys. Rev. Lett. **85**, 4490 (2000).

[38] S. Scheit, V. Averbukh, H.-D. Meyer, N. Moiseyev, R. Santra, T. Sommerfeld, J. Zobeley, and L. S. Cederbaum, J. Chem. Phys. **121**, 8393 (2004).

[39] T. Jahnke, A. Czasch, M. Schoffler, S. Schossler, M. Kasz, J. Titze, K. Kreidi, R. E. Grisenti, A. Staudte, O. Jagutzki, et al., Phys. Rev. Lett. **99**, 153401 (2007).

[40] V. Averbukh, I. B. Müller, and L. S. Cederbaum, Phys. Rev. Lett. **93**, 263002 (2004).

[41] S. D. Stoychev, A. I. Kuleff, F. Tarantelli, and L. S. Cederbaum, J. Chem. Phys. **128**, 104307 (2008).

[42] S. D. Stoychev, A. I. Kuleff, F. Tarantelli, and L. S. Cederbaum, J. Chem. Phys. **129**, 074307 (2008).

[43] K. R. Karim and L. Logan, Physica Scripta **58**, 574 (1998).

[44] C. P. Bhalla, N. O. Folland, and M. A. Hein, Phys. Rev. A **8**, 649 (1973).

[45] K. Kaufmann, W. Baumeister, and M. Jungen, J. Phys. B **22**, 2223 (1989).

[46] J. A. D. Matthew and Y. Komninos, Surf. Sci. **53**, 716 (1975).

[47] D. A. Verner, G. J. Ferland, K. T. Korista, and D. G. Yakovlev, Astrophys. J. **465**, 487 (1996).

[48] M. S. Deleuze, J.-P. Francois, and E. S. Kryachko, J. Am. Chem. Soc. **127**, 16824 (2005).

[49] D. C. Griffin, D. M. Mitnik, and N. R. Badnell, J. Phys. B **34**, 4401 (2001).

[50] In the strict 2p-GF/ADC(2) scheme the $3h1p-3h1p$ block of the interaction matrix $\boldsymbol{C}$ vanishes. The extended 2p-GF/ADC(2)x approximation differs in that the first-order contribution to the $3h1p-3h1p$ interaction is used which would otherwise appear only in the 2p-GF/ADC(3) scheme. In this way the description of the satellite states improves considerably.

[51] We do not consider higher-lying final states, characterized, for example, by four vacancies, an excited electron and an electron in continuum, which can be accessible for initial states of sufficiently high energy. Such final states belong to the $4h2p$ excitation class and cannot be described at the 2p-GF/ADC(2)x level of theory. To describe them ADC(4) would be needed.

TABLES

Configuration	Present	Karim&Logan
$1s^{-1}2s^{-1}\,{}^1S$	275	316
$1s^{-1}2s^{-1}\,{}^3S$	168	203
$1s^{-1}2p^{-1}\,{}^1P$	204	214
$1s^{-1}2p^{-1}\,{}^3P$	213	232

TABLE I: Auger decay widths (in meV) for various electron configurations of doubly ionized neon atom.

	$Ne^{2+}(^1S/D)Ar^+$ (1/2)	$Ne^{2+}(^3P)Ar^+$ (1/2)	$Ne^{2+}(^3P)Ar^+$ (3/2)	Γ_{ICD}	$\tau_{\rm ICD}$
$^1\Sigma$	26.3	0.02	–	26.3	25.0
$^3\Sigma$	1.83	0.35	3.30	5.48	120.1
$^1\Pi$	17.9	0.17	–	18.1	36.4
$^3\Pi$	1.77	0.82	5.61	8.20	80.3

TABLE II: Partial decay widths (in meV, $R_{eq} = 3.5\,$Å) of the $^{1,3}\Sigma$ and $^{1,3}\Pi$ decaying states into different classes of ICD channels. Shown are also the total decay rates (meV) and lifetimes (fs) of these states. For more details, see text.

	$Mg^+Ne^{2+}(^1S/D)$ (1/2)	$Mg^+Ne^{2+}(^3P)$ (1/2)	$Mg^+Ne^{2+}(^3P)$ (3/2)	Γ_{ICD}	τ_{ICD}
$^1\Sigma$	0.75	0.04	–	0.79	833
$^3\Sigma$	0.39	0.08	0.12	0.59	1116
$^1\Pi$	0.29	0.06	–	0.35	1881
$^3\Pi$	0.23	0.08	0.22	0.53	1242

TABLE III: Partial decay widths (in meV, $R_{eq} = 4.4\,\text{Å}$) of the $^{1,3}\Sigma$ and $^{1,3}\Pi$ decaying states into different classes of ICD channels. Shown are also the total decay rates (meV) and lifetimes (fs) of these states.

FIGURE CAPTIONS

FIG. 1: (Color online) Potential energy curves of the doubly and triply ionized states of NeAr relative to the energy of the neutral ground state at equilibrium geometry. The vertical dashed line show the equilibrium internuclear distance, $R_{eq} = 3.5\,\text{Å}$, of the neutral cluster. The groups of curves are discussed in the text.

FIG. 2: Total decay widths and the ETMD partial widths (steeply decreasing curves in the lower left corner) of the singlet states of $Ne^{2+}(2s^{-1}2p^{-1})Ar$ ($\Gamma^{1\Sigma}$, $\Gamma^{1\Pi}$, dashed and dashed-dotted lines) compared to that of $Ne^{+}(2s^{-1})Ar$ (Γ^{2s}, full line). The dotted straight line shows a $1/R^6$ curve normalized to Γ^{2s} at large R. The marked lifetime corresponds to Γ^{2s} at the equilibrium geometry of the neutral cluster.

FIG. 3: The two pathways of the inter-atomic decay of $Ne^{2+}(2s^{-1}2p^{-1})Ar$.

FIG. 4: Total decay widths and the ETMD partial widths (steeply decreasing curves in the lower left corner) of the triplet states of $Ne^{2+}(2s^{-1}2p^{-1})Ar$ ($\Gamma^{3\Sigma}$, $\Gamma^{3\Pi}$, dashed and dashed-dotted lines) compared to that of $Ne^{+}(2s^{-1})Ar$ (Γ^{2s}, full line). The dotted straight line shows a $1/R^6$ curve normalized to Γ^{2s} at large R. The marked lifetime corresponds to Γ^{2s} at the equilibrium geometry of the neutral cluster.

FIG. 5: Selected partial widths of $Ne^{2+}(2s^{-1}2p^{-1})Ar$ Σ (upper panel) and Π (lower panel) initial states. Atomic orbitals notation, valid at large internuclear distances, is used to define the $2h$ and $3h$ states of NeAr.

FIG. 6: (Color online) Potential energy curves of the doubly and triply ionized states of MgNe relative to the energy of the neutral ground state at equilibrium geometry. The vertical dashed line shows the equilibrium internuclear distance, $R_{eq} = 4.4\,\text{Å}$, of the neutral cluster. The potential energy curves of the open $Mg^{2+}(3s^{-2})Ne^{+}(2p^{-1})$ ETMD channels fall into the energy range 46–54 eV and are not shown. The green curves represent the higher lying ETMD channels $Mg^{2+}(2p^{-1}3s^{-1})Ne^{+}(2p^{-1})$ that are closed over the whole range of R.

FIG. 7: Total decay widths and ETMD partial widths (steeply decreasing curves in the lower left corner) of the singlet $MgNe^{2+}(2s^{-1}2p^{-1})$ states ($\Gamma^{^1\Sigma}$, $\Gamma^{^1\Pi}$, dashed and dashed-dotted lines) compared to that of $MgNe^{+}(2s^{-1})$ (Γ^{2s}, full line). The dotted straight line shows a $1/R^6$ curve normalized to Γ^{2s} at large R. The marked lifetime corresponds to Γ^{2s} at the equilibrium geometry of the neutral cluster. The width of the radiative decay of the $Ne(2s^{-1})$ vacancy in free neon atom [49] is shown by the thin horizontal dashed line.

FIG. 8: Total decay widths and ETMD partial widths (steeply decreasing curves in the lower left corner) of the triplet $MgNe^{2+}(2s^{-1}2p^{-1})$ states ($\Gamma^{^3\Sigma}$, $\Gamma^{^3\Pi}$, dashed and dashed-dotted lines) compared to that of $MgNe^{+}(2s^{-1})$ (Γ^{2s}, full line). The dotted straight line shows a $1/R^6$ curve normalized to Γ^{2s} at large R. The marked lifetime corresponds to Γ^{2s} at the equilibrium geometry of the neutral cluster. The width of the radiative decay of the $Ne(2s^{-1})$ vacancy in free neon atom [49] is shown by the thin horizontal dashed line.

FIGURES

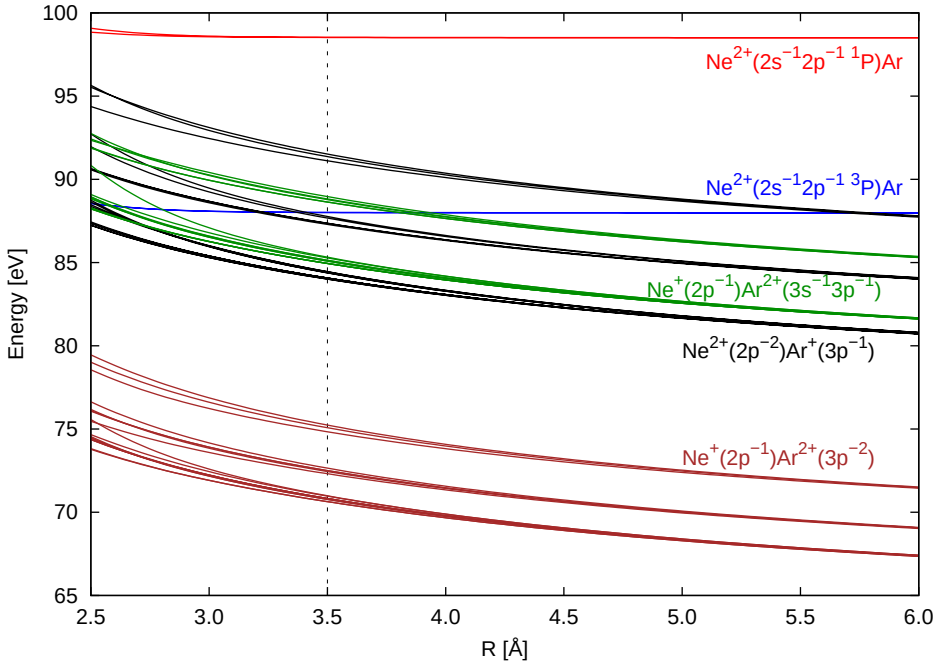

FIG. 1

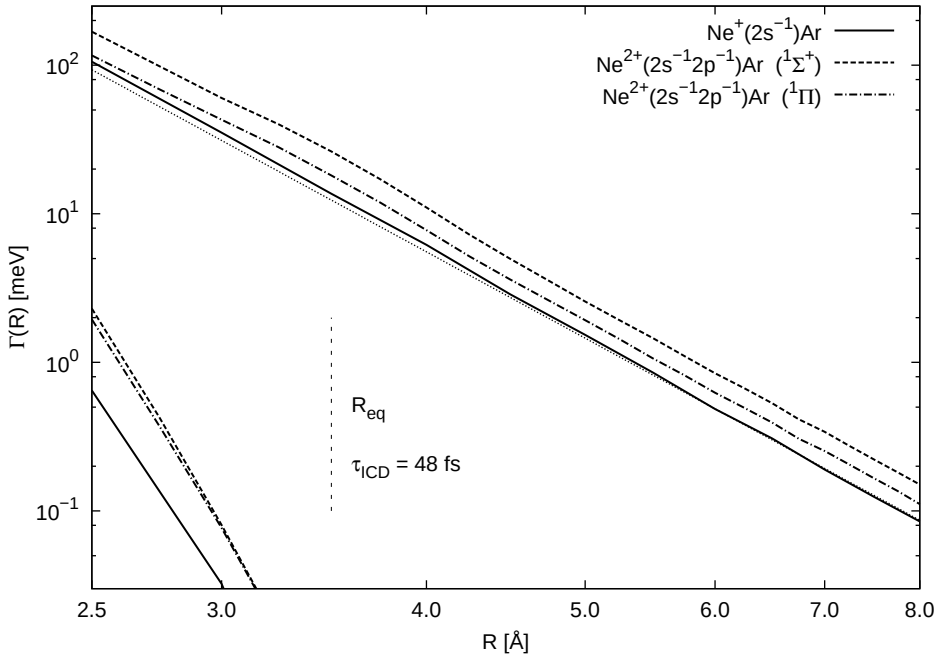
Ne+(2s−1)Ar
Ne2+(2s−1 2p−1)Ar (1Σ+)
Ne2+(2s−1 2p−1)Ar (1Π)
Γ(R) [meV]
10^2
10^1
10^0
10^−1
Req
τICD = 48 fs
2.5
3.0
4.0
5.0
6.0
7.0
8.0
R [Å]

FIG. 2

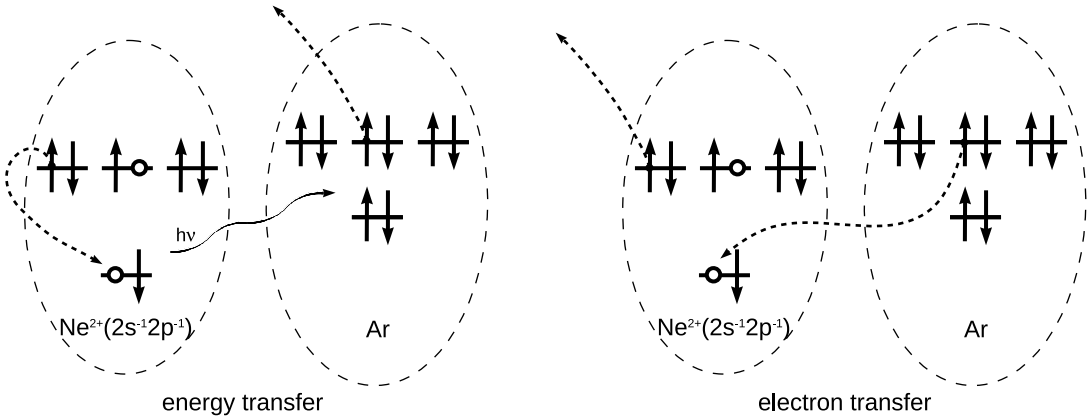
hν
Ne²⁺(2s⁻¹2p⁻¹)
Ar
energy transfer
Ne²⁺(2s⁻¹2p⁻¹)
Ar
electron transfer

FIG. 3

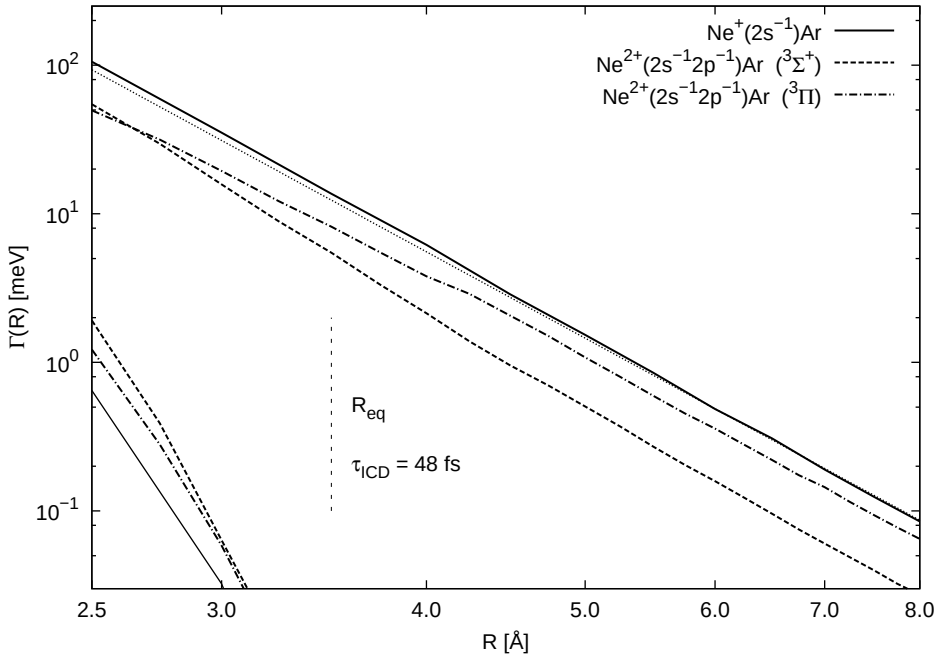
Ne+(2s−1)Ar
Ne2+(2s−1 2p−1)Ar (3Σ+)
Ne2+(2s−1 2p−1)Ar (3Π)
Γ(R) [meV]
10^2
10^1
10^0
10^−1
Req
τICD = 48 fs
2.5
3.0
4.0
5.0
6.0
7.0
8.0
R [Å]

FIG. 4

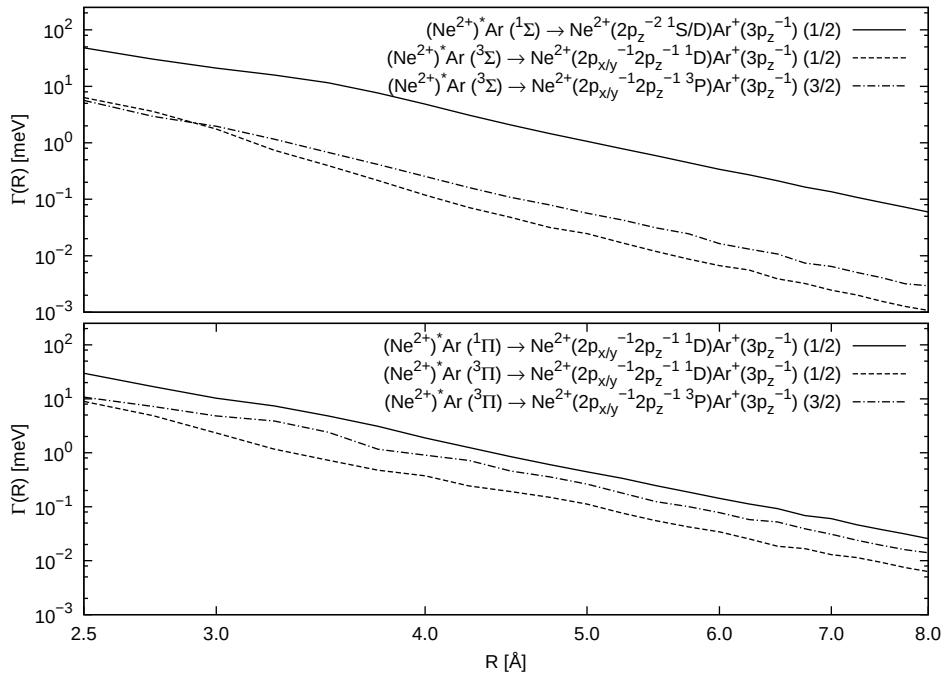
(Ne2+)*Ar (1Σ) → Ne2+(2pz−2 1S/D)Ar+(3pz−1) (1/2)
(Ne2+)*Ar (3Σ) → Ne2+(2px/y−1 2pz−1 1D)Ar+(3pz−1) (1/2)
(Ne2+)*Ar (3Σ) → Ne2+(2px/y−1 2pz−1 3P)Ar+(3pz−1) (3/2)
(Ne2+)*Ar (1Π) → Ne2+(2px/y−1 2pz−1 1D)Ar+(3pz−1) (1/2)
(Ne2+)*Ar (3Π) → Ne2+(2px/y−1 2pz−1 1D)Ar+(3pz−1) (1/2)
(Ne2+)*Ar (3Π) → Ne2+(2px/y−1 2pz−1 3P)Ar+(3pz−1) (3/2)
Γ(R) [meV]
R [Å]

FIG. 5

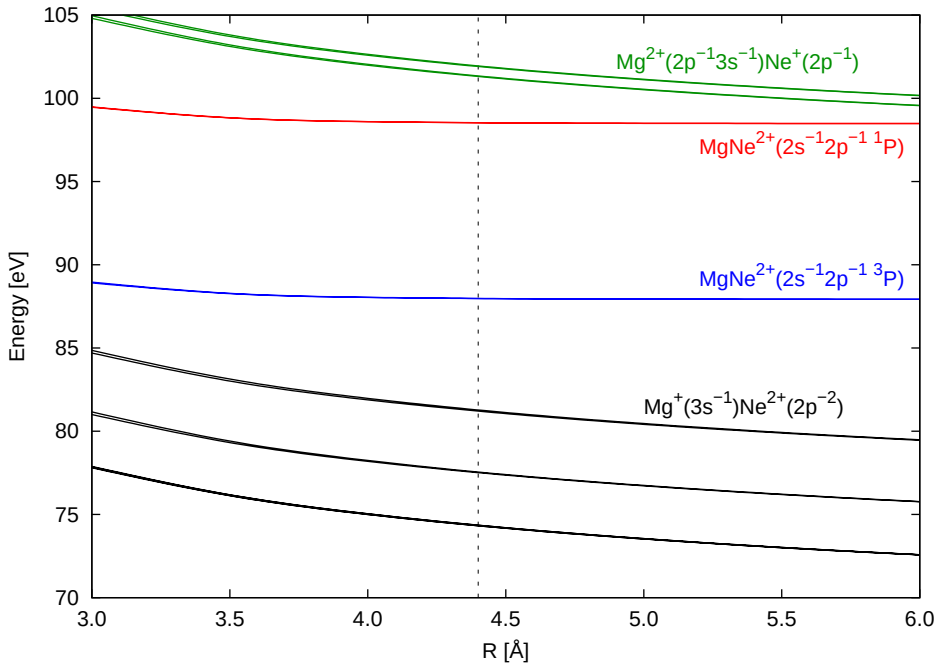
105
100
95
90
85
80
75
70
3.0
3.5
4.0
4.5
5.0
5.5
6.0
Energy [eV]
R [Å]
Mg2+(2p−13s−1)Ne+(2p−1)
MgNe2+(2s−12p−1 1P)
MgNe2+(2s−12p−1 3P)
Mg+(3s−1)Ne2+(2p−2)

FIG. 6

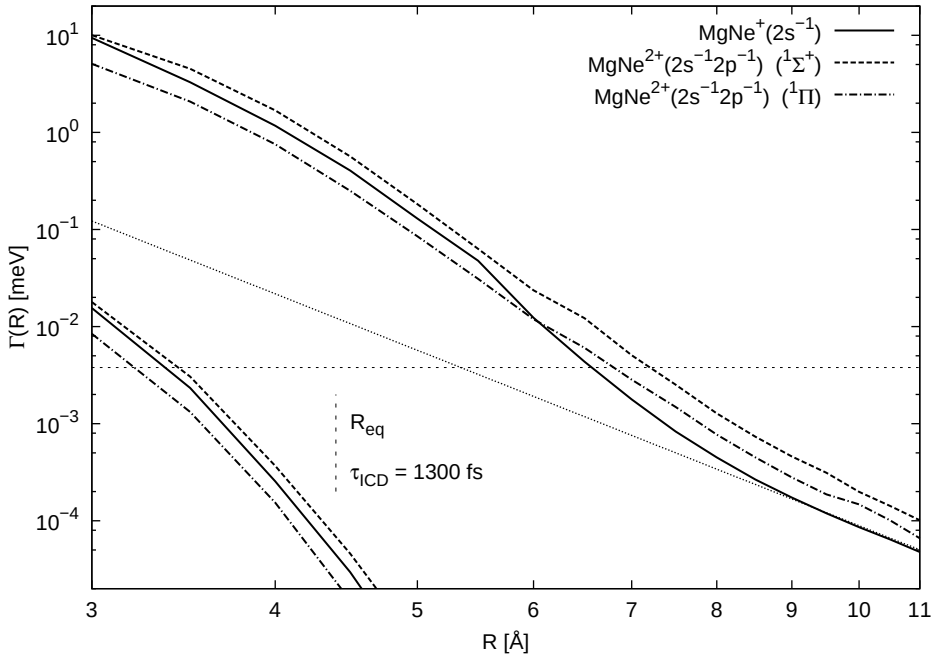
MgNe+(2s−1)
MgNe2+(2s−12p−1) (1Σ+)
MgNe2+(2s−12p−1) (1Π)
Γ(R) [meV]
R [Å]
Req
τICD = 1300 fs
10^1
10^0
10^−1
10^−2
10^−3
10^−4
3
4
5
6
7
8
9
10
11

FIG. 7

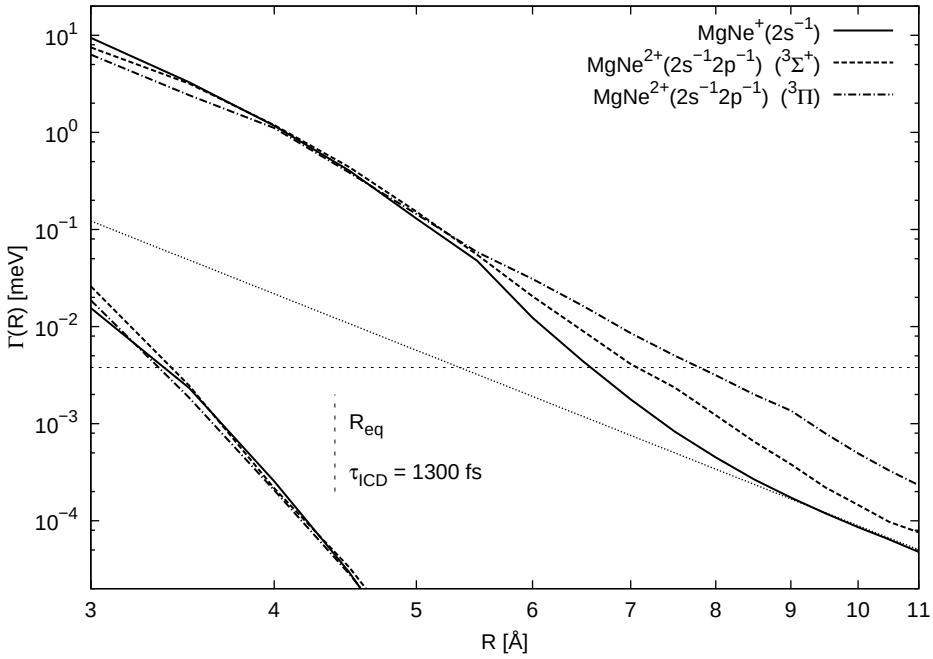
MgNe+(2s−1)
MgNe2+(2s−12p−1) (3Σ+)
MgNe2+(2s−12p−1) (3Π)
Γ(R) [meV]
R [Å]
Req
τICD = 1300 fs
10^1
10^0
10^−1
10^−2
10^−3
10^−4
3
4
5
6
7
8
9
10
11

FIG. 8